Correction of Distributed Optical Aberrations

K. Baker, S. Olivier, C. Carrano, D. Phillion

February 14, 2006

Disclaimer

FY05 LDRD Final Report
Correction of Distributed Optical Aberrations
LDRD Project Tracking Code: 03-ERD-006
Kevin Baker, Principal Investigator

1)   Abstract

The objective of this project was to demonstrate the use of multiple distributed deformable mirrors (DMs) to improve the performance of optical systems with distributed aberrations. This concept is expected to provide dramatic improvement in the optical performance of systems in applications where the aberrations are distributed along the optical path or within the instrument itself. Our approach used multiple actuated DMs distributed to match the aberration distribution. The project developed the algorithms necessary to determine the required corrections and simulate the performance of these multiple DM systems.

2)   Open air Propagation through Distributed Turbulence

2.1 Introduction

In the beginning of this LDRD project, the work was concentrated on looking at the effects of distributed turbulence and correcting this distributed turbulence with a single deformable mirror. As such we built an adaptive optics system which contained an interferometric wave-front sensor and performed open air propagation tests with this system. This work is chronicled in the three papers included in this report as Appendix A, B and C. These tests showed that interferometric wave-fron sensors could be used to correct atmospheric turbulence

Appendix A: K.L. Baker, E.A. Stappaerts, D. Gavel, S.C. Wilks, J. Tucker, D.A. Silva, J. Olsen, S.S. Olivier, P.E. Young, M.W. Kartz, L.M. Flath, P. Kruelevitch, J. Crawford and Oscar Azucena, "High-speed horizontal-path atmospheric turbulence correction using a large actuator-number MEMS spatial light modulator in an interferometric phase conjugation engine," Opt. Lett. 29 1781 (2004). UCRL number: UCRL-JRNL-203988

Appendix B: Kevin L. Baker, Eddy A. Stappaerts, Don Gavel, Jack Tucker, Dennis A. Silva, Scott C. Wilks, Scot S. Olivier, and Jeff A. Olsen, "Adaptive compensation of atmospheric turbulence utilizing an interferometric wavefront sensor and a high-resolution MEMS-based spatial light modulator,"Proc. SPIE 5553, 269-280(2004). UCRL number: UCRL-CONF-206035

Appendix C: K.L. Baker, E.A. Stappaerts, D. Gavel, J. Tucker, D.A. Silva, S.C. Wilks, S.S. Olivier, J. Olsen, "Large-Actuator-Number Horizontal Path Correction of Atmospheric Turbulence utilizing an Interferometric Phase Conjugate Engine," 2004 AMOS Technical Conference, Wailea, Maui, HI (2004). UCRL number: UCRL-CONF-206274

Appendix D: K.L. Baker and S.C. Wilks, "Phase variances arising from a Von Karman turbulence spectrum, unpublished. UCRL number UCRL-JC-151146

3) Multi-Conjugate Adaptive Optics

3.1 Introduction

Correction using multiple deformable mirrors, known as multi-conjugate adaptive optics(MCAO), allows one to obtain to obtain a wider field of view and it also allows the correction of scintillation. The work we performed on MCAO is chronicled in Appendix E. The testbed that was setup included a liquid-crystal spatial light modulator. The work that was performed to calibrate this device is listed in Appendix F. This work also led us to develop a new type of pixilated phase shifting interferometer. The interferometer work is then included in Appendix G.

Appendix E: Kevin L. Baker, Scot S. Olivier, Jack Tucker, Dennis A. Silva, Don Gavel, R. Lim, and Edward J. Gratrix, "Design and progress toward a multiconjugate adaptive optics system for distributed aberration correction," Proc. SPIE 5553, 200-212(2004).UCRL number: UCRL-CONF-206126

Appendix F: K.L. Baker, D.A. Silva, S.S. Olivier and E.A. Stappaerts, "Evaluation of Two-Dimensional Phase Unwrapping Algorithms for Interferometric Characterization of Liquid-Crystal Spatial Light Modulators," submitted to Appl. Opt (2005). UCRL number: UCRL-JRNL-215585

Appendix G: K.L. Baker and E.A. Stappaerts, "Assessment of a Single-Shot, Pixelated Phase-Shifting Interferometer Utilizing a Liquid Crystal Spatial Light Modulator," accepted Opt Lett. (2005). UCRL number: UCRL-JRNL-215836

4) Field Conjugation

4.1 Introdution

Benefits of multiple deformable mirrors in extreme adaptive optics (Direct imaging of extra-solar planets) As an electromagnetic wave propagates through the atmosphere, the phase becomes aberrated due to the atmospheric turbulence. These phase aberrations translate into amplitude aberrations as the wave continues to propagate. This effect, known as scintillation, can then limit the achievable contrast ratios in such demanding applications as extra-solar planet imaging. Through the use of multiple deformable mirrors, however, the scintillation, amplitude variations, can be corrected leading to high achievable contrast ratios.

4.2 Effects of Scintillation on High Contrast Imaging

The effects of scintillation were studied for the Thirty Meter Telescope (TMT) by Fresnel propagating an electromagnetic wave at the science wavelength through the standard seven-layer TMT atmospheric model. This model is shown below in Table 4.2.1. The layer heights, the percentage of the atmosphere at these layer heights and the corresponding Fried parameter, r_o, at the science wavelength of 1.65 μm, is listed in this table. The effective r_o at 1.65 μm is 0.63 m. As the electromagnetic wave propagates

through the turbulence, the phase variations turn into amplitude variations. This occurs over a distance know as the Talbot length, which is dependent on the square of the spatial frequency. The Talbot length is therefore shorter for higher spatial frequencies, however, the energy contained in the higher spatial frequencies is less due to the frequency dependent power spectrum for atmospheric turbulence which leads to a fairly flat contrast ratio.

| Layer height (km)	Percent of Atmosphere	Ro @ 1.65 μm (m)
15.8	0.015	7.8
13.1	0.082	2.8
7.4	0.025	5.7
5.8	0.035	4.7
3.3	0.119	2.3
1.8	0.078	2.9
0.0	0.646	0.8

Table 4.2.1 Seven layer TMT atmospheric model.

After propagating the electromagnetic wave through the seven-layer atmospheric model, the resulting pupil is scintillated. By placing an apodization mask in that plane and performing a Fourier transform, the field in the Fourier plane is determined. The instantaneous contrast ratio can be determined by squaring the field to get the intensity and looking at the resulting lineout. For these tests, a prolate spheroid mask was chosen for the apodizer as shown in Fig. 4.2.1. This apodizer allows for contrast ratios of 10^{-11} to be achieved along the horizontal axis as shown below as the solid black line in Fig. 4.2.1.
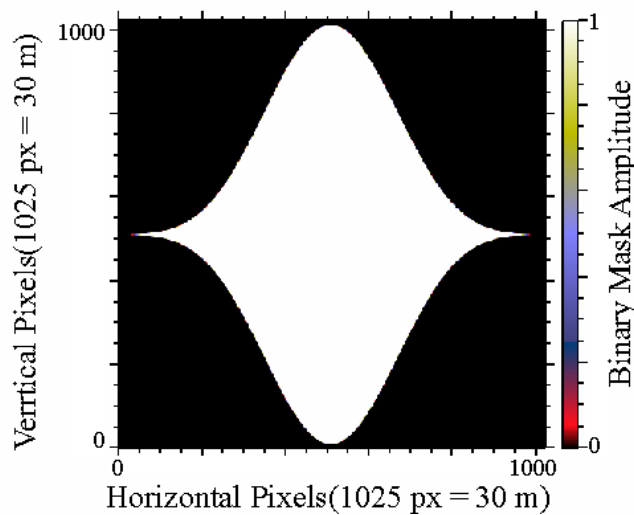
Figure 4.2.1 Binary mask used for the apodizer.

Two separate codes were used to generate the atmospheres. An IDL program was used to generate a Von Karman turbulence spectrum with an outer scale of $L = 2\pi/\kappa_0 = 25$ m and ARROYO was used to generate a Kolmogorov turbulence spectrum. Both codes used an effective r_0 of 0.63 m at 1650 nm. The 1650 nm light, after Fresnel propagation through the screens, had an intensity in the pupil as shown in Figure 4.2.2 for the ARROYO code.
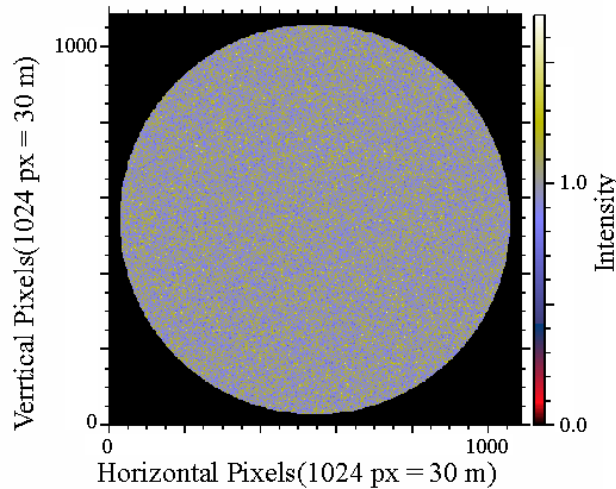
Figure 4.2.3 Intensity scintillation at 1650 nm from the ARROYO simulation.

A complex wave consisting of the field corresponding to the intensity pattern in Figure 4.2.3, a zero phase component and the apodization mask shown in Fig. 9.4.1.1 was then used to determine the point-spread-function and from that the instantaneous contrast ratio. The resultant point-spread-function is shown below in Fig. 9.4.1.3.
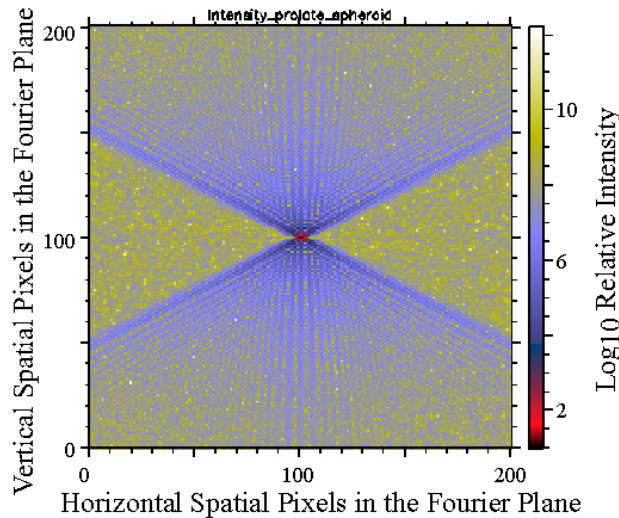
Figure 4.2.3 Far-field image of scintillated pupil apertured with the apodizer above.

A horizontal lineout through the center of the Far-field image above shows that the instantaneous contrast ratio due to scintillation alone is $\sim 10^{-7}$, dashed line in Fig. 4.2.4. This contrast ratio was obtained for both the ARROYO code using a Kolmogorov spectrum and the IDL code using a Von Karman spectrum. The contrast ratio is fairly flat over the 100 λ/D plotted(2 pixels $\sim \lambda/D$).
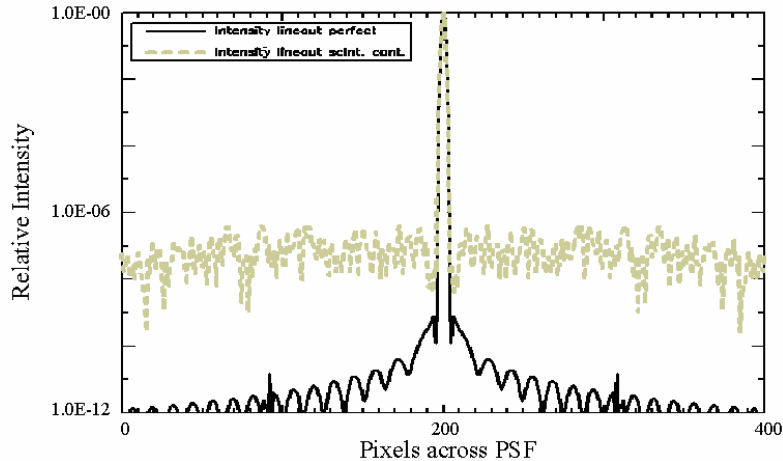
Figure 4.2.4 Relative intensity lineout of Arroyo generated intensity at the pupil.

4.3 Effects of Chromaticity on High Contrast Imaging

The chromatic effects associated with Fresnel propagating two wavelengths through the atmosphere were also studied. This is of interest in the case where the science wavelength and the wave-front senor at different wavelengths. Chromatic effects will limit the contrast ratio achievable. This effect was again studied by Fresnel propagating two electromagnetic waves, one at the science wavelength of 1.65 μm and another at the wave-front sensor wavelength of 0.85 μm, through the standard seven layer TMT atmospheric model. Due to the wave-length dependence of the Fried parameter, the shorter wavelength electromagnetic wave passes through stronger turbulence and is hence more scintillated than the longer wavelength electromagnetic wave. This difference in the scintillation between the two wavelengths will result in differences in the phase at the pupil for the different electromagnetic waves.

The IDL code was used to generate pupil fields at two wavelengths and therefore allowed an evaluation of the effects of chromaticity and also allowed a comparison between the relative importance in chromatic phase and scintillation. The two field generated had their phases wrapped modulo 2π and so before the difference in phase could be determined the phases were unwrapped using a path-following algorithm. To study the effects of chromatically induced contrast ratio alone, a uniform field was generated with the apodizer mask shown in Fig. 4.2.1 applied and the difference between the phases of the two wavelengths was used for the phase. Fourier transforming the field and finding the intensity allowed this effect to be examined. The instantaneous contrast ratio due to chromatic Fresnel propagation is shown below in Figure 4.3.1 as the solid black line. In this case the instantaneous contrast ratio due to chromatic Fresnel propagation is below 10^{-9} as far out as 30 λ/D.
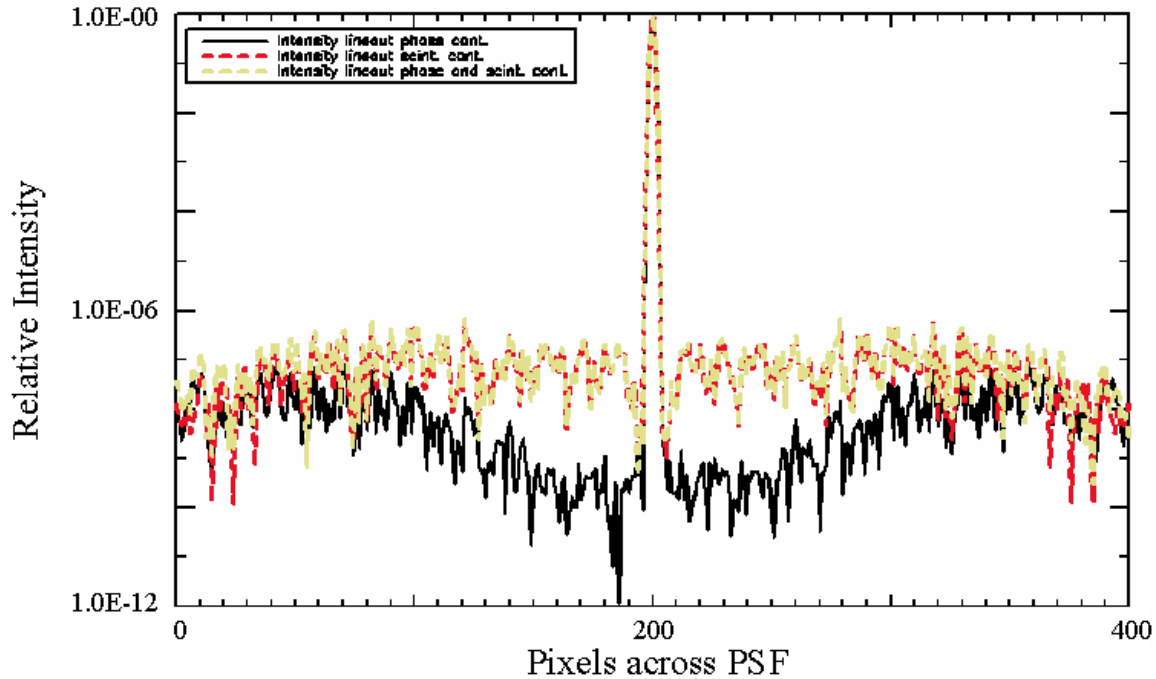
Figure 4.3.1 Contrast limitations due to scintillation and chromatic phase differences.

Figure 4.3.1 also has the total instantaneous contrast ratio due to both chromatic Fresnel propagation, dashed yellow line, and due to scintillation, dashed red line. This plot shows that scintillation is more important than chromatic Fresnel propagation for this particular case out to~60 λ/D. The scintillation contrast limit of 10^{-7} agrees with the contrast above from the Arroyo simulations which had a similar variance in the intensity at the pupil. That indicates that by correcting for the intensity variations in the beam, that much higher contrast ratios could be obtained.
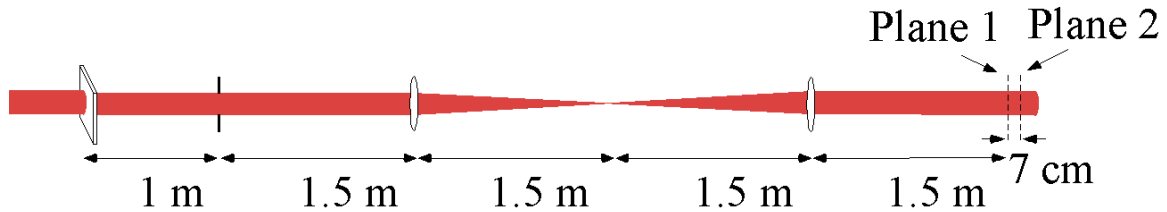
4.4 Field Correction

In this LDRD project we developed a new technique for field conjugation, both amplitude and phase. The field correction is achieved with multiple deformable mirrors. The new technique which we developed is doing field correction using the Transport of Intensity equation (TIE). This approach can be used in extreme adaptive optics to obtain high contrast. It can also be implemented in short pulse laser systems. For the case of short pulse laser systems, phase compensation increases the intensity on target and amplitude compensation allows greater energy to be delivered on target. An improvement in intensity of as much as an order of magnitude could be expected.

An example of method is shown below. In this simulation, light passes through a phase screen that is located a meter in front of the entrance pupil of the telescope as shown in Figure 4.4.1. The beam becomes scintillated after passing through the phase screen, Kolmogorov turbulence spectrum. The pupil is then relay imaged to the first deformable mirror, plane 1, and then passes to a second deformable mirror, plane 2. The concept behind the algorithm is to measure the intensity and phase in the first plane. In the second plane it is desired to have a uniform beam. This algorithm uses the Transport of intensity equation, along with the intensity measurement in the first plane to determine what phase

needs to exist in the first plane such that given the intensity present in the first plane, a uniform intensity will be generated at the second plane upon propagation. It then uses the measured phase in the first plane and applies the difference between the desired phase and the measured phase to the DM such that the desired phase is placed upon the beam after reflection from the first DM. Figure 4.4.2 presents three different cases of initial scintillation going from left to right. The intensity in the first plane , second plane and the intensity in the second plane after application of the correct phase in plane 1. and the resulting intensity at the second plane after one iteration. In each of the three cases the peak intensity was dropped by a factor of two and the variance in the intensity was dropped by a factor of three.

Figure 4.4.1 Simulation setup for the field correction.
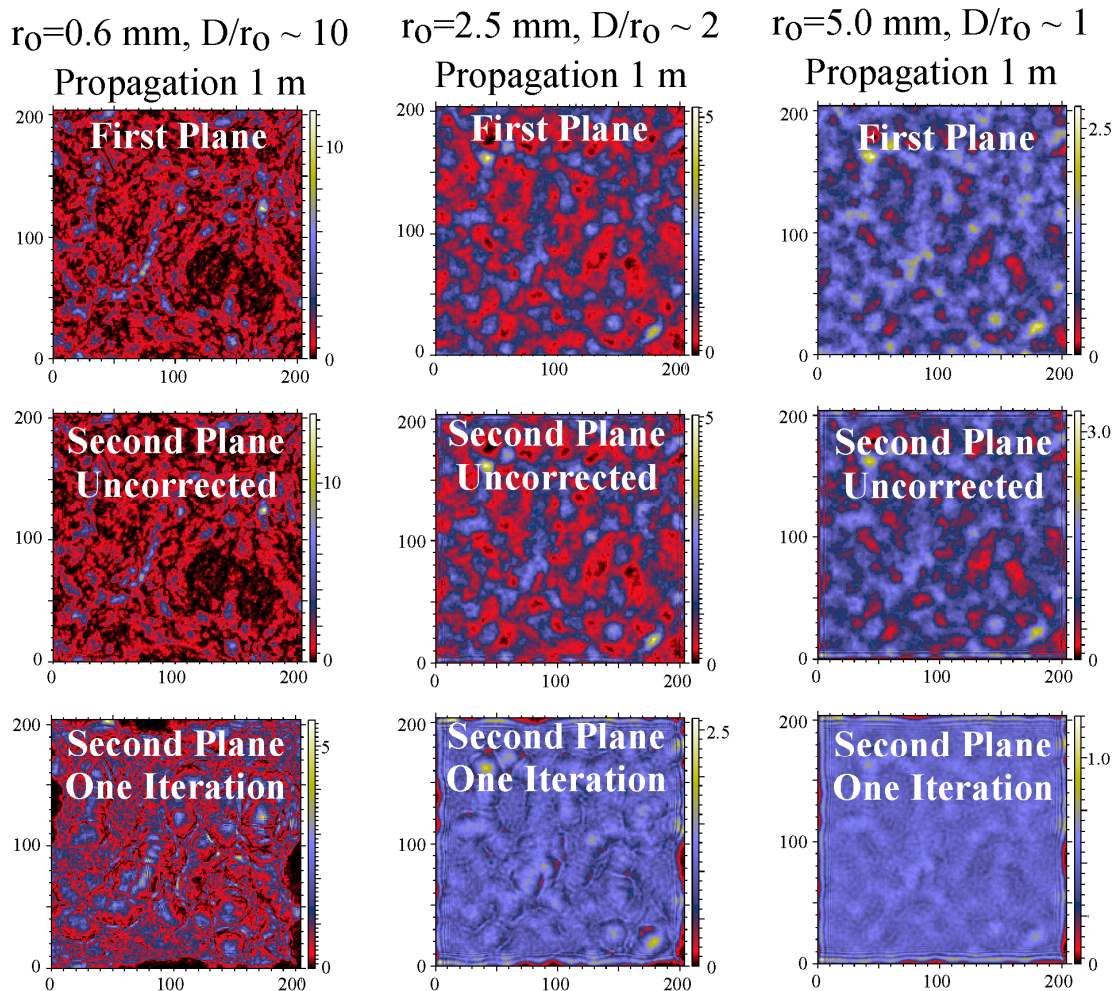
Figure 4.4.2 Simulation results for the Field correction code.

Techniques for dealing with telescope with multiple deformable mirrors:

5)   Large Synoptic Survey Telescope(LSST)

5.1 Introduction

5.2 Wave-front sensing for the LSST

5.2.1 Introduction:
A Shack-Hartmann based wave-front sensor is considered below for the LSST telescope. For simplicity and reliability, the desire is to arrive at a wave-front sensor that has no moving components and does not have to be changed relative to the focal plane array when the spectral filters are changed.

5.2.2 Principles of operation of a Shack-Hartmann wave-front sensor:
A Shack-Hartmann wave-front sensor is composed of a lenslet array placed in the pupil of the optical beam being measured. The lenslet array is composed of an array of identical lenslets, each of which measures a small portion of the optical beam. A CCD camera is placed one focal length, f.l., behind the lenslet array. A plane wave incident on the lenslet array produces an array of focal spots located on the optical axis of the individual lenslets. An aberrated beam produces a local gradient in the phase, $\nabla\phi$, across each of the lenslets, displacing the focal spots from the optical axis as shown in Figure 5.2.2.1. Each individual spot is displaced from the center of the lenslet by a distance $s = (\nabla\varphi)(f.l.)\lambda/2\pi$, where λ is the wavelength of the incident light, as illustrated in Figure 5.2.2.2. Therefore, the Shack-Hartmann wave-front sensor measures the wave-front gradient with a spatial resolution equal to the sub-aperture size. At minimum, a quad cell is required to measure the two-dimensional wave-front tilt.

If the source of illumination for the Hartmann sensor is a point source, as in a traditional Hartmann sensor, then the spot displacements are typically found using a "center-of-mass" calculation on the intensity. If there is an extended scene illuminating the pupil, then the scene displacements at each of the sub-apertures is measured by performing cross-correlations between the scenes in the separate sub-apertures. The latter technique was pioneered by the solar adaptive optics community and is the more likely technique to be used for the LSST telescope if the pupil of the telescope is reimaged beyond the focal plane array.
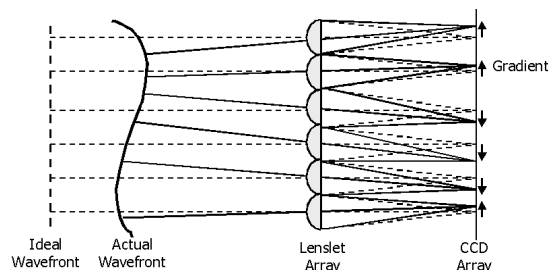

Figure 5.2.2.1 Illustration denoting hypothetical Hartmann spots from a plane wave, dashed lines, and a severely aberrated beam, solid line.
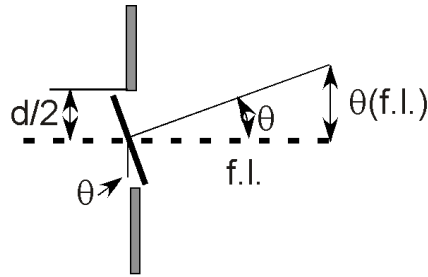
Figure 5.2.2.2 Principle of operation of each lenslet. The angular displacement of the spot for each individual lenslet indicates the average slope vector of the wave-front across the given lenslet.

5.2.3 Design considerations:

The plate scale on the detector is 0.2 Arcseconds. The diffraction limited spot size on the WFS should be approximately equal to the pixel size of the detector or $2.44\lambda f/\# = 4 - 10 \ \mu m$. At 400 nm the f/# should then be between 4 and 10. If the WFS is operating at f/4 then the maximum angular range entering the lenslet array should be less than 14 degrees to exclude cross-contamination between lenslets. That then in turn limits the field stop that can be used. The schematic of the wave-front sensor with a conventional lens is shown in Figure 5.2.3.1. In this case a 5 mm f.l. lens is used to form an image of the pupil onto a lenslet array. In this case, the field stop has to be (14 degrees)(5 mm/ 10.5 m)=6.7x10-3 degrees or 117 pixels or 0.39 arcminutes across the focal plane array such that signal from adjacent lenslets do not mix. The correlation or conventional Hartmann sensor would then let in a field of 0.39 arcminutes to do the wave-front sensing. It would require a multi-element lens with a focal length of ~5 mm that would accept the f/1.25 beam from the telescope and provide correction over the exit angle of the ~collimated light leaving the lens at +/- 7 degrees.

LSST Telescope

Focal
Plane
Array

10.5 m   10.5 m

Correlation
Wave-front
Sensor

Focal
Plane
Array
Plane

5 mm f.l.
aspheric
lens

WFS

Field
Stop

5 mm 5 mm   Lenslet
Array

Field stop-0.39 Arcminutes-117 pixels on fpa-1.17 mm square
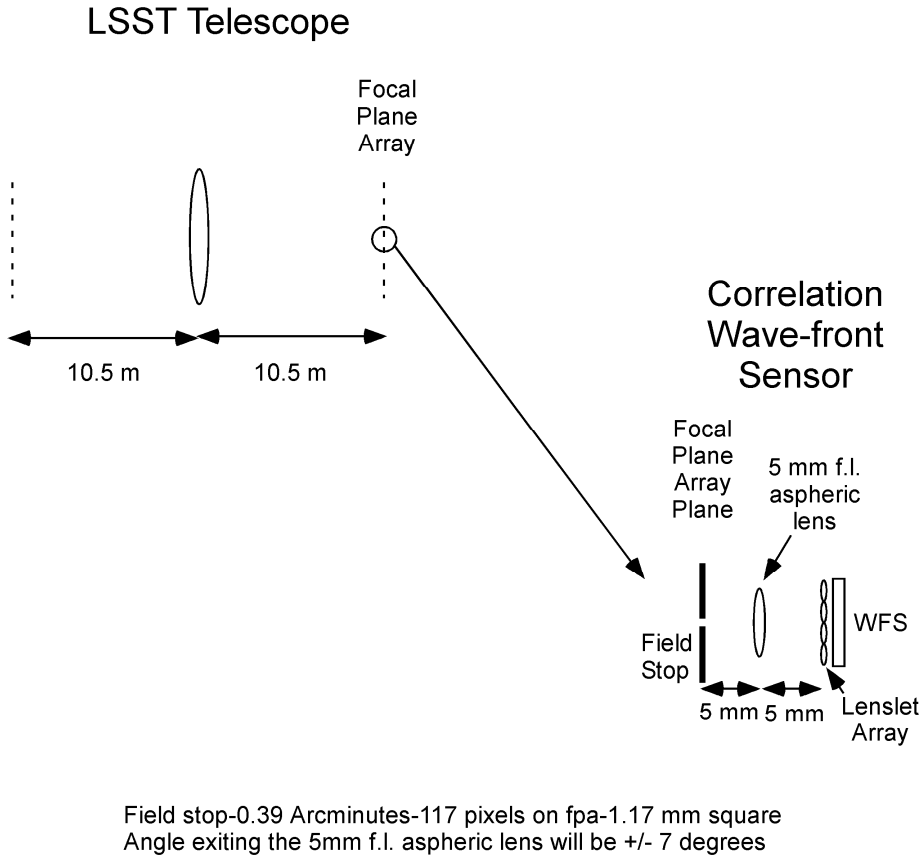Angle exiting the 5mm f.l. aspheric lens will be +/- 7 degrees

Figure 5.2.3.1 Schematic for Shack-Hartmann wave-front sensing.

5.2.4 Lens design:

   An optimization for the 5 mm f.l. lens was performed. The result was an f/1.25, 5.0 mm EFL, 1.17 mm square focal plane coverage with near diffraction limited performance over the 400-1040 nm spectral band. The lens is telecentric at FP and does not require any lens motion or focal plane shift for filter changes. The lens is composed of two triplet lenses in which the first surface of the first triplet and both outer surfaces of the last triplet are aspheres. Triplets with 3 different glasses are required to get the broad chromatic correction. The length between the lenslet array and the focal plane is approximately 19 mm. The lens gives good performance at 200 lp/mm. One could also consider the use of Gradium lenses as well, perhaps even for the lenslet array.

5.2.5 Expected photon flux from stars of a given magnitude:

   The number of photons per second collected by the telescope is given by D.J. Schroeder, *Astronomical Optics* (Academic Press, San Diego, 2000)

$$R_p = 10^{11} * T_a * D^2 * \Delta\lambda * 10^{-m/2.5},$$

where 10^{11} is the number of photon/sec from a magnitude 0 star, T_a is the atmospheric transmission coefficient(assume 0.7), D is the effective diameter of the telescope(LSST=6.9 m effective), $\Delta\lambda$ is the bandpass of the filter(assume 0.12 μm) and m

is the magnitude of the star. For a sixteenth magnitude star, the number of photons per unit time incident upon the pupil will be 1.59×10^5 photons/sec or 1.6 million photons in the 10 second integration window. (An 18th mag. would be $10^{-2/2.5}$ or 0.16 times as many photons and a 20th mag. would be $10^{-4/2.5}$ or 0.025 times as many photons) There is then the transmission loss through the telescope, the quantum efficiency of the detector array, the number of subaperture arrays, the number of CCD pixels/subaperture array. If the final image of the aperture is 4 mm, then it will be spread over an area of 400x400 CCD pixels, with at most 50 % containing signal due to the pupil geometry. If the pupil is sampled by 24 lenslets across the pupil, then there will be 16.67 by 16.67 CCD pixels per lenslet subaperture. The size of the psf on the focal plane array by a give star will be $2.44(\lambda/r_o)$f.l.=2.44(4e-7/0.2)(8.4*1.25)=51 μm. The angular spread falling on the image of the pupil will be the atmospheric spreading multiplied by the ratio of the focal lengths or (λ/r_o)(f.l. tele/f.l.)= (λ/r_o)(8.4*1.25/5.e-3). The spot size on the wave-front sensor will then be the angular spreading multiplied by the focal length of the lenslet. The focal length of the lenslet is set by the desired angular range of the field of view to be f/4 and the focal length of the lenslet is then (f/4)(diam.)=f/4(4mm/24)=667 μm. The spot size on the lenslet will then be $2.44(\lambda/r_o)$(8.4*1.25/5.e-3)f/4(4mm/24)=2.44(4e-7/0.2)(8.4*1.25/5.e-3)f/4(4mm/24)=6.67 μm. This would then necessitate small pixels(5 μm) for classical Hartmann sensing. The star then falls on essentially four pixels within each lenslet(want a quadcell) due to atmospheric blurring, and we desire to have at least 50 photons per pixel, then we need at least 200 photons per subaperture with approximately $0.5*(24)^2$ subapertures or 57,00 photons. That would then require an approximate magnitude 19.6th star to run the AO system, assuming a magnitude 20 star would provide 40,000 photons to the telescope.

5.2.6 Availability of stars:

The graph for the star density used in this section was taken from J. W. Hardy, *Adaptive Optics for Astronomical Telescopes* (Oxford University Press, New York, pg. 356, 1998). Specifically the graph is shown in Figure 4a. The star density is lower in the galactic pole than in the galactic equator and hence the galactic pole will be used to determine if sufficient stars are present. A field of view of 0.39 arcminutes represents a solid angle of $\pi\theta^2$ or π(0.39 arcmin(1rad/57.3 deg)/(60 arcmin/deg)) ^{2}=4.0x10^{-8} sr. According to Figure 4 below, this solid angle should yield a single star of visual magnitude 16 at the galactic equator. There would not likely be suitable stars at the galactic pole. At 1.56 arcmin(4 wave-front sensors together), there would be a single star of visual magnitude 14 at the galactic equator and 20 at the galactic pole.

Star Densities

A average star density model
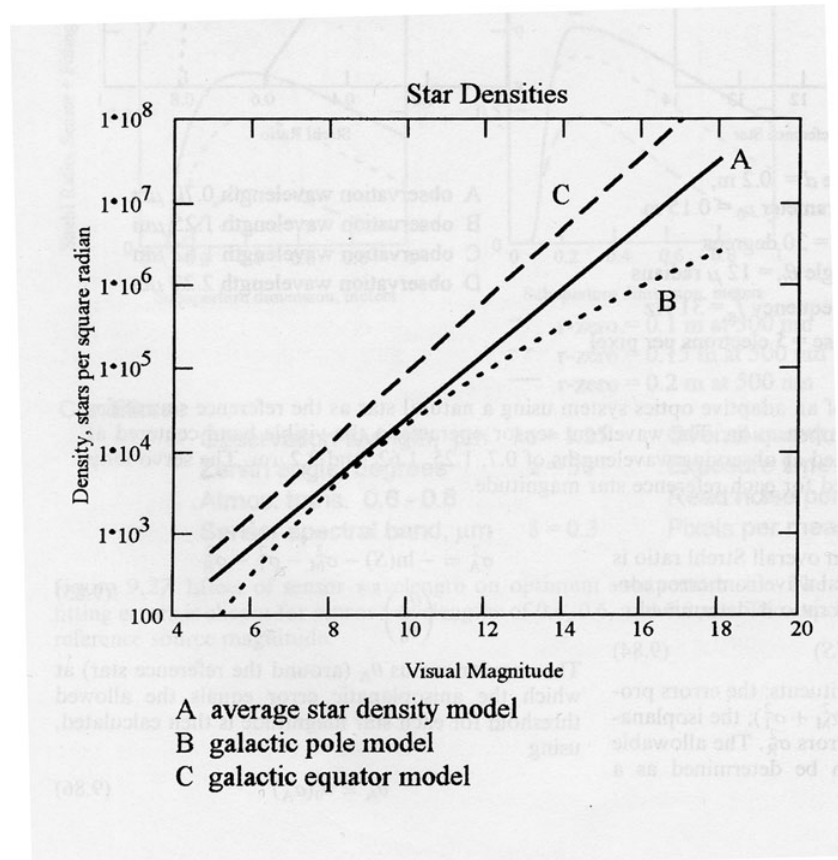B galactic pole model
C galactic equator model

Figure 5.2.6.1a Density of stars brighter than a given visual magnitude. Models for the galactic pole and equator are based on data from Wolfe, W.L. and G.L. Zissis (Eds.), *The Infrared Handbook* (Environmental Research Institute of Michigan, Ann Arbor, 20-22 1985).

      The probability of finding a star of given magnitude is more pessimistic in the graph shown in Figure 5.2.6.1b. This graph is technically only valid for 16th magnitude stars and brighter. In this case to get a 95% chance of seeing a star of visual magnitude 18 at a galactic latitude of 90 degrees, then you would require a field-of-view with a diameter of approximately 210 arcseconds. The design described above has a field of view of 24 arcseconds, which would require about 17 detectors to achieve a field of view of 100 arcseconds. Sixteen detectors, 4x4 array, would require a 2 cm square area for collection. Having redundant detectors, or an array of detectors, has the advantage if multiple stars can be found then multiple measurements of the mirror aberrations can be averaged to reduce the noise and help take out residual atmospheric aberrations.. For the estimated 19.6[th] magnitude star estimated above and 16 redundant detectors in a 4x4 array such that the field of view is increased to ~100 arcseconds, there would be a roughly 60% chance of seeing a star at a Galactic latitude of 90 deg. (solid lines), an ~ 80% chance of seeing a star at 45 deg. (long-dashed lines), and a greater than ~95% chance of seeing a star at 30 deg. (short-dashed lines).
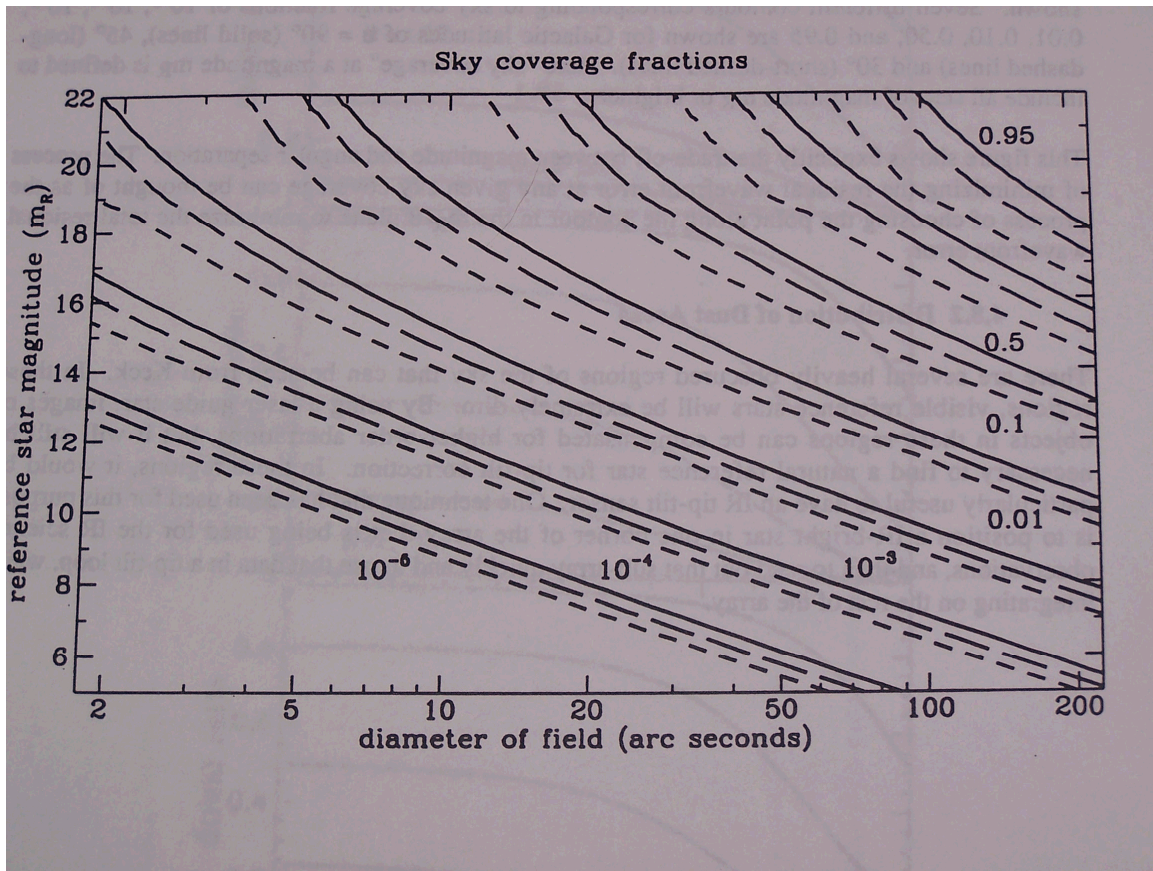
Figure 5.2.6.1b Sky coverage fractions (labels on curves) as a function of reference magnitude m_R and angular separation radius θ in μrad. The data, derived from the model of JN Bahcall and RM Soniera, "The distribution of stars to v=16th magnitude near the north galactic pole- normalization, clustering, and counts in various bands," Astrophysical Journal 246 (1) pg. 122-135 (1981), are shown for a Galactic latitude of 90 deg. (solid lines), 45 deg. (long-dashed lines), and 30 deg. (short-dashed lines). The horizontal axis is twice the angular separation between an astronomical object at a random place on the sky, and the nearest star that is brighter than or equal to the magnitude shown. For example, to obtain a 95 % sky coverage fraction with an 18th-magnitude reference star at the galactic pole, one would typically be at a radius of about 110 arc seconds from that reference star. Graph is taken from Keck Observatory report no. 208, "Adaptive optics for Keck observatory," pg. 4-100 (1994).

5.2.7 Diagnostic calibration:

The reference spots for the Hartmann sensors could be obtained by making a simple fixture that would fit in the 1 cm by 1 cm slot and hold a fiber optic at the axial location of the focal plane array centered on the Hartmann wave-front sensor. The fiber optic would be several microns in diameter and would provide the reference spots from which the Hartmann sensor would drive its errors to in closed loop. Problem would be the close proximity of the final lens to the focal plane location.

5.2.8 Mirror coverage on the LSST telescope:

–15–

The primary mirror on the LSST telescope has an outer radius of 4.2 m and an inner radius of 2.53 m. The secondary has an outer radius of 1.6 m and the tertiary has an outer radius of 2.5 m. a ray trace of the marginal rays for the 3.5 degree field-of-view short design is shown in Figure 5.2.8.1. The mirror coverage at each of the three mirrors for rays along the optical axis of the telescope are shown in Figure 5.2.8.2, 5.2.8.3 and 5.2.8.4 for the primary, secondary and tertiary mirrors, respectively. The primary mirror has complete coverage on axis as there is no vignetting, however, vignetting becomes significant at large field angles. Likewise there is good coverage on the secondary and tertiary mirrors as well.
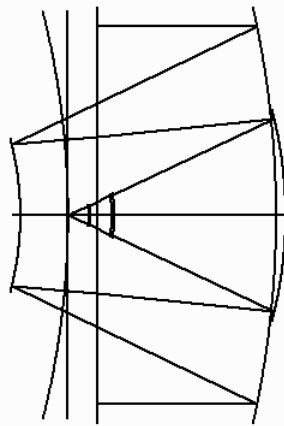

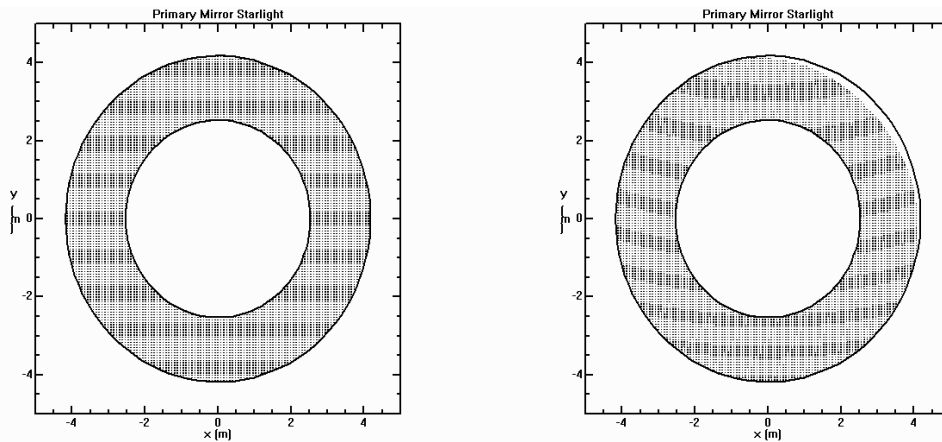Figure 5.2.8.1 Ray trace of the marginal rays through the LSST telescope.

Figure 5.2.8.2 Coverage of the primary mirror at zero field angle and at 1.2 degrees.
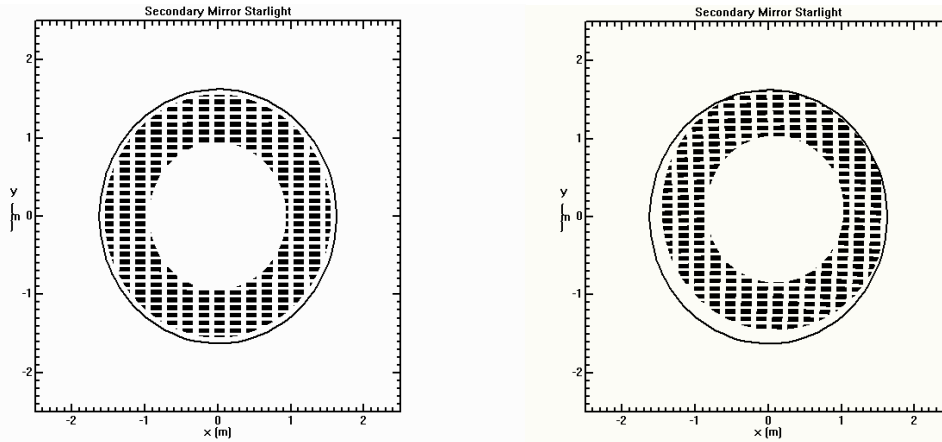
Figure 5.2.8.3 Coverage of the secondary mirror at zero field angle and at 1.2 degrees.
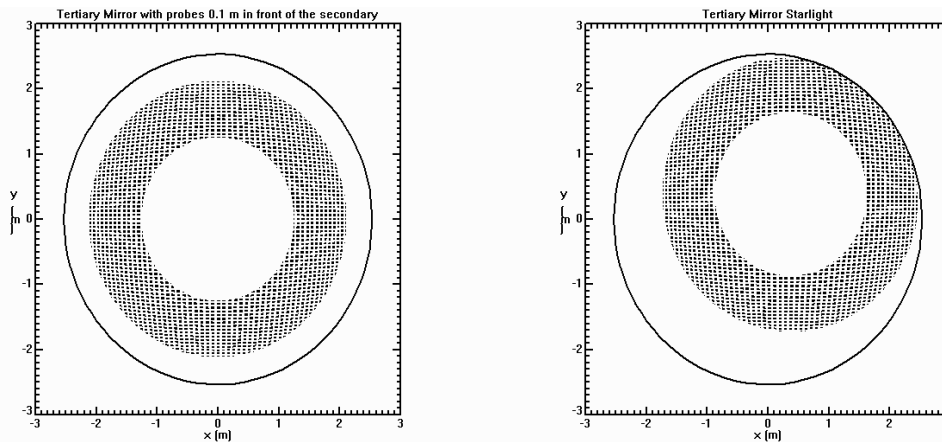
Figure 5.2.8.4 Coverage of the tertiary mirror at zero field angle and at 1.2 degrees.

5.2.9 Alternate GRIN lens design:

Additionally a GRIN lens could be used in place of the aspheric lens. The GRIN lens would accept a wide angular spectrum and produce an image of the pupil at the output. The GRIN lens would produce an image of the pupil at the size of the input field into the GRIN lens. Therefore, a given GRIN lens can take a 0.39 arcminute field and produce a pupil image at that size, 1.17 mm. The small image of the pupil size would require a very small lenslet pitch, ~ 50 μm, to accurately sample the pupil. The angular spectrum leaving the GRIN lens would be close to f/1.25 and these lenses are not achromatic. This would then require the lenslet array to have a comparably fast f/# to prevent leakage between the adjacent lenslets and the combination of the GRIN lens and the lenslet array to be somewhat achromatic.(Could a large array of GRIN lenses be used as a fast lenslet array? The fill factor would likely be low, ~50% due the ray paths through the GRIN lens as shown in Figure 5.2.9.1. Sufficient sampling would require the lenslets to be ~50 μm whereas the smallest diameter that I have seen commercially is 500 μm.) A large number of these GRIN lenses can be used to create a very large field-of-view, greatly enhancing the possibility of seeing a star. A 2 mm diameter GRIN lens could have a field-of view of 24 arcseconds and in the space of 2 cm by 2 cm, an array of

–17–

10x10 GRIN lenses could be implemented providing 100 separate wave-front detectors for an effective field-of-view of 240 arcseconds. If there is only a single star in the aperture, then traditional Hartmann sensing can be implemented. If there are multiple objects, then correlation sensing can be implemented. The GRIN lenses will, however, suffer chromatic aberration.
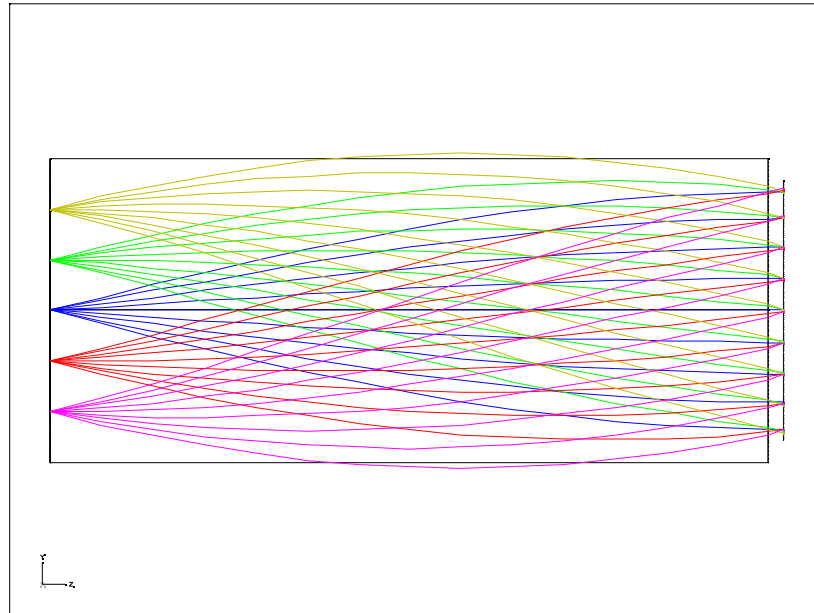
Figure 5.2.9.1. Grin lens replacement for the aspheric lens.
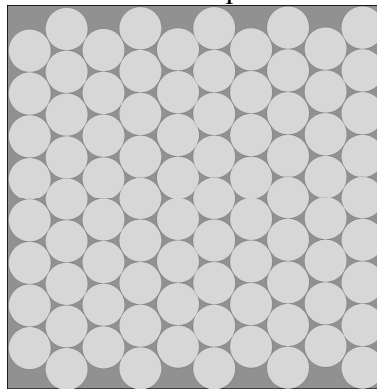
Figure 5.2.9.2. Grin lens array to produce a large field-of-view.

5.2.10 Initial simulations of a Shack-Hartmann wave-front sensor for the LSST geometry:

Simulations of a Shack-Hartmann wave-front sensor with 23 lenslets across the LSST pupil are shown below. In this case the pupil size on the lenslet array is 4 mm such that each lenslet represents 0.37 m on the primary mirror and there are 4 x 4 CCD pixels per lenslet in the simulations. The atmospheric properties were such that the wind speed was 20 m/sec and the Fried parameter is listed below each set of images. The integration time was 30 sec with 0.1 sec acquisition intervals. In the simulations below, the tilt was removed under the assumption that the focal plane array would be moved around to eliminate wind shake of the telescope and atmospheric tip/tilt effects.
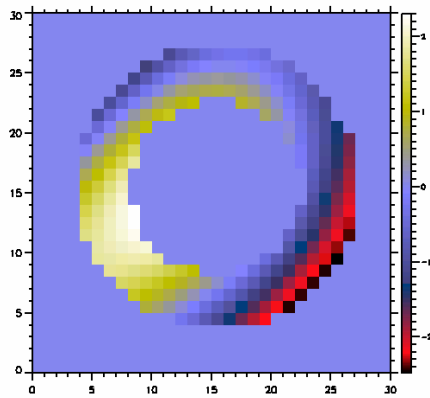
Initial Phase (rad)
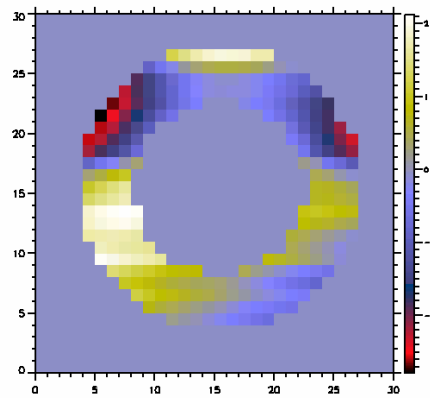
Reconstructed Phase (rad)
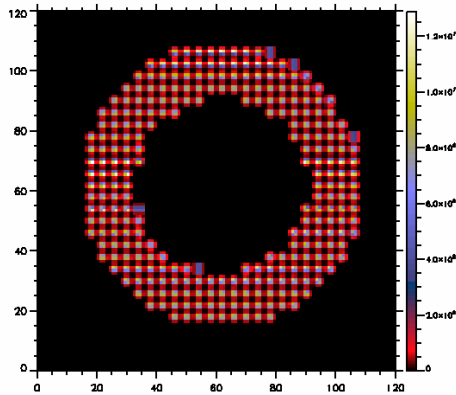
Hartmann Spots

Figure 5.2.10.1 Shack-Hartmann simulations of the LSST Telescope

5.2.11 Spinoffs

A number of wave-front sensors were tested for the LSST telescope with the Shack-Hartmann giving the most encouraging results. This led to several papers on the use of these wave-front sensors in other applications, Appendix H, and in new algorithms for the Shack-Hartmann wave-front sensor, Appendix I.

Appendix H: K.L. Baker, "Curvature wave-front sensors for electron density characterization in plasmas," Rev. Sci. Instr. 74, 5070 (2003). UCRL number: UCRL-JRNL-155323

Appendix I: K.L. Baker, "Least-Squares Wave-Front Reconstruction of Shack-Hartmann Sensors and Shearing Interferometers using Multigrid Techniques," Rev. Sci. Instrum. 76, 053502 (2005). UCRL number: UCRL-JRNL-209572

5.3 Tomography on the LSST

In order to correct the aberrations on the LSST telescope, the correct aberrations must be mapped to the appropriate mirrors.

5.3.1 LSST Alignment Strategy

Least squares SVD is used to obtain the desired mirror deformations and the desired rigid body motions from the wavefront sensor wavefronts. The most important point to remember is that provided we obtain near ideal imaging across the entire field, it does not matter whether the optical system ends up as designed or not. It can happen that the magnitude of the mirror deformations and the magnitude of the rigid body motions is the same before and afterwards, only that now these represent a null mode which gives good wavefronts over the entire field.

We make the conservative assumption that wavefront sensor pistons and tilts are unobservable. Only one iteration is required in the ideal world where the sensitivity matrix is known precisely, where the control system is completely linear, and where there is no noise. We also have two sets of wavefront sensors, one which is used for the fitting and the other which simply goes along for the ride. In this way we can confirm that we have achieved good wavefronts over the entire field, not just at a set of wavefront sensor positions.

The sensitivity matrix has one part due to the mirror deformations and another part due to the rigid body motions. The part due to the mirror deformations can either be calculated using the analytic Zernike transformations or by ray tracing. The rigid body motions part of the sensitivity matrix is always calculated by ray tracing. When ray tracing, parallel ray bundles to the wavefront sensors are first traced for the ideal optical system. The cluster points of the focused ray bundles in image space are determined and the sets of Zernike coefficients representing the far field wavefronts in image space are calculated. Note that this procedure does not give the Zernike coefficients for piston, tilts, and focus. These are what we call the reference wavefronts and the reference cluster points. The ray trace code has the ability to apply Zernikes to the surfaces and to translate and rotate the surfaces. One perturbation at a time is applied to the optical system and, for each perturbation, parallel ray bundles are ray traced to the wavefront sensors. As before, the cluster points of the focused ray bundles in image space are determined and the sets of Zernike coefficients representing the far field wavefronts in image space are calculated. The columns in the sensitivity matrix are determined be taking differences of sets of Zernike coefficients except that, for each perturbation, the Zernike coefficients representing tilts and focus are obtained from the shift in position of the cluster point. A perturbation is defined as one Zernike being applied to one surface or one surface being given one motion. (The exception to this is when the primary and tertiary mirrors are fabricated together. Then we work with combined motions).

The ability to do iterations has been added. This is important to determine if there is walk-off. We look both at the rms bendings of the three mirrors versus iteration and at the rms changes in bendings of the three mirrors versus iteration. We have defined a metric for the rigid body misalignment. Using that metric, we look at the rigid body

misalignment metric versus iteration and the rigid body misalignment metric for the changes in the rigid body motions versus iteration.

This shows that the alignment strategy essentially converges in one iteration and that there is only a slight improvement in the second iteration. The alignment does not walk off.

A strong independent corroboration of the alignment strategy was sought. For this reason, after each iteration, the mirror deformations and rigid body motions are applied and ray traces are done for the parallel ray bundles for the wavefront sensors. This has shown that starting with a 1 mm rms spot radius, we can achieve a 10 micron spot radius. The ideal system has an average spot radius of about 3 microns over the field.

We also have the capability to add noise to the wavefront sensors. Currently this noise can either derive from a Komolgorov turbulence phase screen at an altitude or be white noise. We also have the ability to randomly omit a specified number of wavefront sensors at each iteration. Also, the noise can be made dynamic by randomly changing the signs of the Zernike coefficients for the wavefront sensor errors at each iteration.

We have discovered that only five wavefront sensors are required. If good wavefronts are obtained for five wavefront sensors spread over the field, then it is guaranteed that the wavefronts are good across the entire field. This is true even if all the possible degrees of freedom are included as actual degrees of freedom. The possible degrees of freedom include the mirror deformations, the mirror rigid body motions, and the ccd motions for z and tip/tilt.

5.3.2 Tomographic code developed for LSST

5.3.2.1 Introduction

Least squares SVD is used to obtain the desired mirror deformations and the desired rigid body motions from the wavefront sensor wavefronts. The most important point to remember is that provided we obtain near ideal imaging across the entire field, it does not matter whether the optical system ends up as designed or not. It can happen that the magnitude of the mirror deformations and the magnitude of the rigid body motions is the same before and afterwards, only that now these represent a null mode which gives good wavefronts over the entire field.

5.3.2.2 Operation – Choosing settings
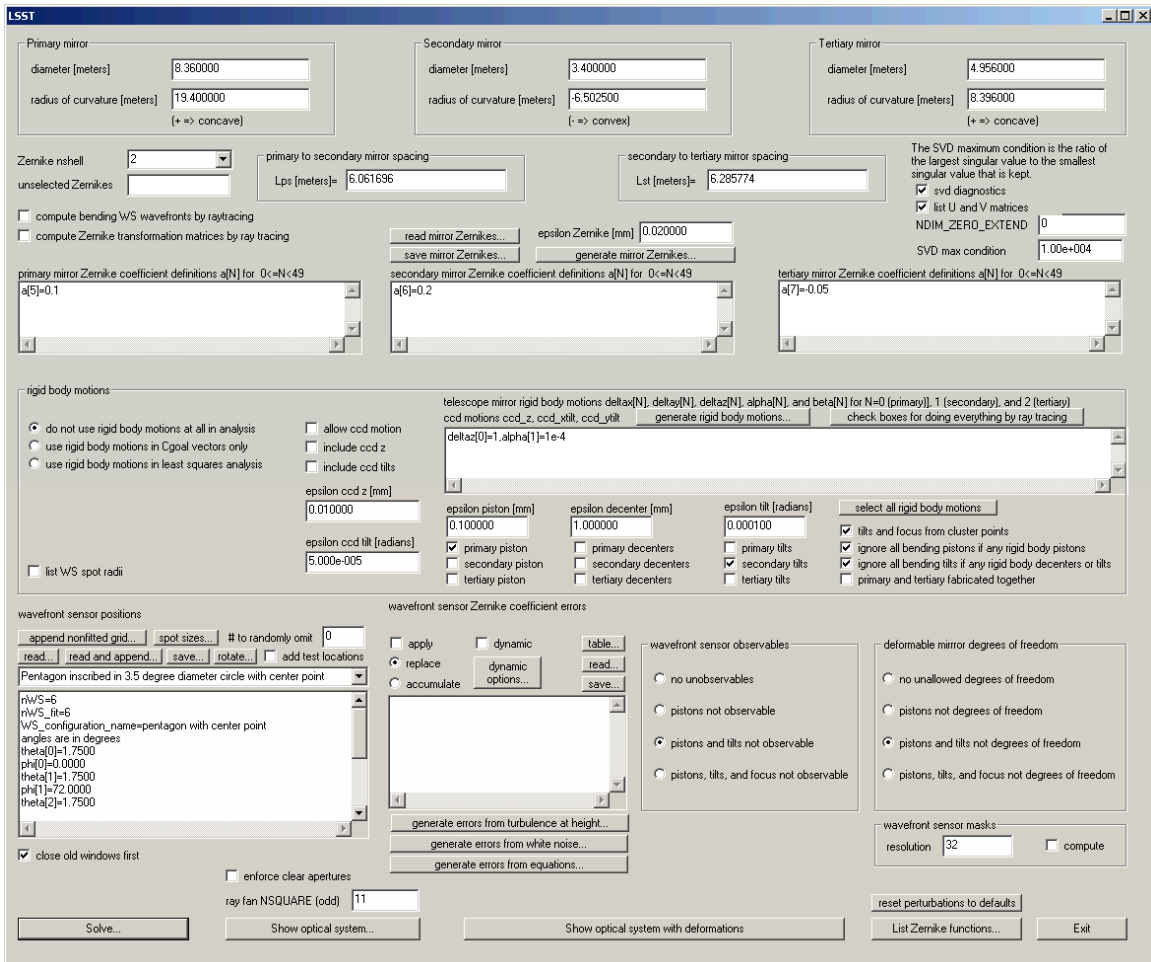
Starting from the top of the window:

5.3.2.3 The physical dimensions of the telescope

The current LSST design is the default setting in the program for the three mirrors:

	Diameter [meters]	Radius of curvature [meters]
Primary mirror	8.360000	19.400000
Secondary mirror	3.400000	-6.502500
Tertiary mirror	4.956000	8.396000

Primary to Secondary mirror spacing [meters]	6.061696
Secondary to tertiary mirror spacing [meters]	6.285774

5.3.2.4 Zernike nshell

The number of Zernike polynomials used in the least squares SVD is determined by the value of nshell (and the wavefront sensor observables).

The number of Zernike terms is equal to $(nshell+1)^2$. Both the normalized and unnormalized terms can be displayed by the "List Zernke functions" button at the bottom right hand side of the LSST window. For example, when nshell = 2 (the default condition), there are 9 Zernike terms and they are as follows:

```
Unnormalized Zernike functions
  N    n    m    equation
  0    0    0    1
  1    1    1    R*cos(A)
  2    1   -1    R*sin(A)
  3    1    0    2*R^2-1
  4    2    2    R^2*cos(2*A)
  5    2   -2    R^2*sin(2*A)
  6    2    1    (3*R^2-2)*R*cos(A)
  7    2   -1    (3*R^2-2)*R*sin(A)
  8    2    0    6*R^4-6*R^2+1

Normalized Zernike functions
  N    n    m    equation
  0    0    0    sqrt(1)*(1)
  1    1    1    sqrt(4)*(R*cos(A))
  2    1   -1    sqrt(4)*(R*sin(A))
  3    1    0    sqrt(3)*(2*R^2-1)
  4    2    2    sqrt(6)*(R^2*cos(2*A))
  5    2   -2    sqrt(6)*(R^2*sin(2*A))
  6    2    1    sqrt(8)*((3*R^2-2)*R*cos(A))
  7    2   -1    sqrt(8)*((3*R^2-2)*R*sin(A))
  8    2    0    sqrt(5)*(6*R^4-6*R^2+1)
```

Notes:
1. All Zernike coefficients in the LSST code are for the unnormalized Zernike functions
2. The normalized Zernike functions are normalized so that the integrals of their squares over the unit circle are pi.

One may also choose to exclude certain Zernike terms from the deformable mirror degrees of freedom by entering the appropriate numbers into the "unselected Zernikes" box. (Note that for certain terms (piston, tilts, focus), this can be done equivalently by selecting a button in the deformable mirror degrees of freedom area.)

5.3.2.5 SVD max condition

The SVD max condition determines the ratio of the largest singular value to the smallest singular value that is kept. Testing has shown that while using raytracing, for nshell = 2, the best choice for the SVD max condition is 10^4 and for nshell = 3, the best choice is 10^5. These SVD conditions are automatically entered by the program immediately after selecting either nshell = 2 or 3 (although the option remains to be able to change the condition after nshell is chosen). For other values of nshell (0, 1, 4, 5, 6), care should be taken to determine an appropriate value of the SVD max condition to use. Including more singular value terms than necessary (max condition is too large) will add extra

null modes to the mirror reconstructions and the mirrors will be bent more than necessary. If the max condition is too small, the mirrors will not be allowed to be bent into the proper shape for correction? To view the singular values, check the "svd diagnostics" box (default condition = checked).

5.3.2.6 List U and V matrices

These are the matrices from the SVD and were diagnostics for checking the operation of the program which are not directly useful.

5.3.2.7 NDIM_ZERO_EXTEND

The number entered in this box increases the number of columns of the sensitivity matrices. This option was included for testing the code, and does not ever need to be touched.

5.3.2.8 Raytracing

The sensitivity matrix has one part due to the mirror deformations and another part due to the rigid body motions. The part due to the mirror deformations can either be calculated using the analytic Zernike transformations or by ray tracing.

To use ray tracing, check the "compute bending WS wavefronts by raytracing" and "compute Zernike transformation matrices by ray tracing" boxes.

The rigid body motions part of the sensitivity matrix is always calculated by ray tracing. When ray tracing, parallel ray bundles to the wavefront sensors are first traced for the ideal (as-designed) optical system. The cluster points of the focused ray bundles in image space are determined and the sets of Zernike coefficients representing the far field wavefronts in image space are calculated. Note that this procedure does not give the Zernike coefficients for piston, tilts, and focus. These are what we call the reference wavefronts and the reference cluster points. The ray trace code has the ability to apply Zernikes to the surfaces and to translate and rotate the surfaces. One perturbation at a time is applied to the optical system and, for each perturbation, parallel ray bundles are ray traced to the wavefront sensors. As before, the cluster points of the focused ray bundles in image space are determined and the sets of Zernike coefficients representing the far field wavefronts in image space are calculated. The columns in the sensitivity matrix are determined be taking differences of sets of Zernike coefficients except that, for each perturbation, the Zernike coefficients representing tilts and focus are obtained from the shift in position of the cluster point. A perturbation is defined as one Zernike being applied to one surface or one surface being given one motion.

5.3.2.9 Mirror bending perturbations − Zernike coefficient definitions

A perturbation to the wavefronts at each of the three telescope mirrors can be applied. There are three boxes for the Zernike coefficient definitions, one for each of the three mirrors. The deformations applied in these boxes are to the wavefronts at the mirrors, not the mirrors themselves. The actual mirror deformation is smaller by a factor of two.

The coefficients may be entered in a variety of ways:

- Generated by equation
- Individually entered manually
- Read in from text file

To generate the mirror Zernike coefficients by equation, click on "generate mirror Zernikes" and a window will open. In this window, you may type in equations for the coefficients of the unnormalized Zernikes using the following format:

a_primary[N] = f[N]
a_secondary[N] = f[N]
a_tertiary[N] = f[N]

f[N] has units of millimeters and N is the zero-based coefficient number. (e.g. For nshell = 2, N = [0, 1, 2...8].)

The current default equations create Zernike coefficients with a power law distribution and random sign (modeled after residual aberrations from another telescope after correction):

```
execute("random_seed(1)",N==0)
f_primary=0.1,f_secondary=0.2,f_tertiary=-0.05
Npower=max(N,1)^-1.2447
a_primary[N]=(N>2)*f_primary*random_sign()*Npower
a_secondary[N]=(N>2)*f_secondary*random_sign()*Npower
a_tertiary[N]=(N>2)*f_tertiary*random_sign()*Npower
```

In the "Generate mirror Zernikes" window, it is also possible to read and save the Zernike equations, which should prove useful when better estimated LSST mirror defomations become available.

After generating the mirror coefficients by equation, the individual coefficients appear in each of the three mirror Zernike coefficient definition boxes in the main LSST window. If desired, the coefficients can be manually modified or entered for each of the mirrors in the form a[N] = number.

If there is a set of Zernike coefficients for the wavefront deformations at each of the mirrors that will be often used, it can be saved and read in by the appropriate buttons in the LSST window.

Still need to describe the epsilon Zernike [mm] box._____

5.3.2.10 Rigid body motions

In the rigid body section of the LSST window, one has three choices of ways to allow the program to run, each selectable by a radio button:

- do not use rigid body motions at all in analysis
- use rigid body motions in Cgoal vectors only
- use rigid body motion in least squares analysis

If the first button is selected, none of the rigid body perturbations will be read in and there will be no rigid body motions of the mirrors allowed in the SVD corrections

If the second button is selected, it will be possible to perturb the rigid body motions of the mirror, but there will be no allowed rigid body degrees of freedom for correction. (The Cgoal vectors (one for each wavefront sensor) describe the desired wavefront of each wavefront sensor in the image plane by Zernike coefficients.)

If the last button is selected, the mirrors can have rigid body motions as initial perturbations and as correctable degrees of freedom. If this button is selected, a check box will appear which gives you the option of only having rigid body motions (no deformable mirror degrees of freedom). If the box is checked to have rigid body motions only, two more radio buttons appear. These allow you to choose between allowing the original deformable mirror perturbations to be corrected or not.

The telescope rigid body perturbations for all three mirrors and the CCD are entered into the same box. The mirror rigid body motions are use the following names: deltax[N], deltay[N], deltaz[N] for the x, y, and z translations and alpha[N] and beta[N] for the x and y tilts. (Only two tilts since the system is rotationally symmetric.) Here, N designates the mirror: N=0 (primary), N=1(secondary), and N=2 (tertiary).

(Perhaps the program should be changed to have "MIRROR" instead of "N" here in the LSST window to eliminate confusion with Zernike #, as in the window that shows up for generating rigid body motions by equation.)

Important: if the box is checked to fabricate the primary and tertiary mirrors together, only the primary mirror rigid body motions will be read in by the program. Currently, the tertiary mirror will be given the same perturbations as the primary. This will soon be changed to allow for fabrication errors.

There are three CCD motions allowed as perturbations: ccd_z, ccd_xtilt and ccd_ytilt. (x and y decenters appear very much as x and y tilts and so are not included.)

The rigid body motions can be generated by equation, just as the deformable mirror Zernike coefficients. Also, as with the mirror Zernike coefficients, both the equations for generating the coefficients and the coefficients themselves can be saved or read as text files. As with everywhere else in the program where not explicitly labeled, the units of distance are mm. The tilts are in units of radians.

5.3.2.11 Rigid body motions – degrees of freedom

The rigid body degrees of freedom of the telescope can be each selected individually. Each of the three mirrors can allow either piston, decenters or tilts. However, if the box is checked to allow the primary and tertiary mirrors to be fabricated together, the options for the tertiary mirror disappear.

For convenience, there is a box to click which will allow you to "select all rigid body motions" at the same time.

Description of the epsilon pistons, decenters and tilts_____

If the appropriate box is checked, tilts and focus will be from the cluster points. Otherwise, tilts and focus are calculated from _____.

There are also boxes for the option of ignoring all bending pistons if any rigid body pistons and bending tilts if any rigid body decenters or tilts. If these boxes are not checked, then all the motions are added together. ???

5.3.2.12 Wavefront sensor positions

The location of the wavefront sensors is entered in the box in the bottom left hand corner of the LSST window. Two sets of wavefront sensors can be included; one which is used for the fitting and the other which simply goes along for the ride. In this way we can confirm that we have achieved good wavefronts over the entire field, not just at a set of wavefront sensor positions. The wavefront sensors are entered according to their angular positions, theta and phi in degrees. There is a drop-down menu which allows commonly tested configurations to be quickly chosen and entered. Other configurations may be saved and loaded using the buttons.

The total number of wavefront sensors needs to be defined in the first line in the window. For example, "nWS=6" tells the program to look for six wavefront sensors defined as theta[n] and phi[n] for n = 0 to 5. The next line in the box needs to define the number of wavefront sensors used for the fit. If the value for nWS_fit is the same as that for nWS, then there will be no nonfitted wavefront sensors which "go along for the ride."

Any locations can be used as nonfitted wavefront sensor locations. However, there is one array of nine wavefront sensor test locations often used. If the "add test locations" box is checked before the wavefront sensor configuration is chosen in the drop-down menu, the nine test locations will be added automatically. If you wish to add the test locations after choosing a configuration, you can do so with the "read and append" button. This button is useful for adding the three wavefront sensor test locations (which is faster to run than the nine test locations). While using "read and append," the text files that are read in should have the nWS be the number of wavefront sensors defined in the file. The nWS value in the window will be changed to the sum of the previous value of nWS and file nWS value, and the wavefront sensors in the file will be appended to the window with the appropriately changed wavefront sensor numbers.

For some configurations of wavefront sensors, there seems to be a dependence on the rotation of the wavefront sensors. For this reason, there is an option for rotate the fitted, nonfitted or all of the wavefront sensors by some angle, given in degrees.

It is assumed that each wavefront sensor has a star in its field of view. To simulate the condition of unavailable stars, a number of wavefront sensors may be omitted from the fit. When the "# to randomly omit" is nonzero, the given number will be randomly omitted from the set of fitted wavefront sensors. The nonfitted wavefront sensors will not be affected.

There is something that needs to be fixed in the code here. The wavefront sensors are not listed as omitted if there are less than 5 WS remaining- due to the fact that we previously thought a minimum of 5 WS were required.

5.3.2.13 Spot sizes

When this button is clicked, a table of spot sizes for each wavefront sensor will be generated. The sizes will be calculated by using exact ray tracing for the full LSST optical system for each wavefront sensor's parallel bundles of rays.

5.3.2.14 Noise

We also have the capability to add errors, or noise, to the wavefront sensors. Currently this noise can either derive from 1) a Komolgorov turbulence phase screen at an altitude, 2) white noise or 3) be generated by equation. To apply the noise, be sure to check the "apply" button. Also, the noise can be made dynamic using one of three different options. You can: 1) randomly change the signs of the Zernike coefficients for the wavefront sensor errors before each iteration which is very quick, but not very realistic, 2) generate new phase screens each time (very slow) or 3) generate new Zernike coefficients by using the current values as the one sigma values in a Gaussian distribution. To be able to have both noise from a turbulence phase screen and white noise, you can

check the "accumulate" button before generating the new noise Zernike coefficients.

Reminder: The coefficients listed in this window are for the unnormalized Zernikes and the units are in mm.

After clicking "generate errors from white noise," a window will open. In this window, you can choose nshell for the noise (the default is set to match the value of nshell chosen for least squares SVD.), the rms value of the noise (Zernike coefficients added in quadrature) and a random seed. There is an option to exclude Zernike terms so that noise is not added to the terms you are not observing. In this way, you can keep the total amount of noise on the observed terms consistent, even with different values of the random seed. The default condition for the excluded Zernikes is set to match the wavefront unobservables (see next section).

Turbulent phase screens. Add Karhunen-Loeve terms to fix low-order Zernike terms. (Karhunen-Loeve terms make corrections over a circular aperture, so the size of the original phase screen is increased by a factor of sqrt 2. The corrections work over the inscribed circle of the enlarged square and then the final corrected phase screen is the square inside the circle.)

5.3.2.15 Wavefront sensor observables

In this section, you can choose the unobservable Zernike terms. The choices are:

- no unobservables (used for diagnostics, not physical)
- pistons not observable (info never available from wavefront sensors)
- pistons and tilts not degrees observable (good choice for LSST)
- pistons, tilts, and focus not observable (comment, when to use?)

As the default condition, we make the conservative assumption that wavefront sensor pistons and tilts are unobservable.

5.3.2.16 Deformable mirror – degrees of freedom

In the bottom right hand corner of the window, there are radio buttons to choose the degrees of freedom allowed for correction:

- no unallowed degrees of freedom
- pistons not degrees of freedom
- pistons and tilts not degrees of freedom
- pistons, tilts, and focus not degrees of freedom

The current default condition is that pistons and tilts are not degrees of freedom because piston and tilts are chosen as wavefront sensor unobservables. There is no need to correct what you can't see….

It is also possible to unselect certain Zernike terms, such as piston (0) , tilts (1,2) and focus (3), by typing in the term numbers in the box underneath the nshell.

5.3.2.17 Miscellaneous

There are more checkboxes and controls in the bottom of the LSST window:

- "close old windows first" is useful, especially when doing multiple iterations.
- "list WS spot radii" will make the program calculate and list spot radii for each wavefront sensor. Be sure to select this box before solving. If this box is not checked during solves or iterations and then checked before iterating again, there will be entries earlier in the table that are zeros.
- "enforce clear apertures" will cause rays to be blocked by the central obscurations. (Rays that don't go through the circular entrance pupil are always blocked, regardless of the state of this check box.) Even when this box is not checked, clear apertures are enforced for the spot radii calculations
- "ray fan NSQUARE (odd)" tells the program how many rays to trace. (The default is 11.
  11^2=121. Subtracting the rays at the corners of the square that don't make it through the circular aperture leaves around 97 rays total used in the ray tracing
- STILL NEED TO DESCRIBE WHY/WHEN TO USE THESE NEXT ONES
- "change deformations and rigid body motions to solution or solution deviation"
- "Show optical system"
- "change deformations and rigid body motions to solution or solution deviation"
- "Show optical system with deformations and rigid body motions"
- "wavefront sensor masks" and resolution
- "reset perturbations to defaults"

5.3.2.18 Solve

When all the settings have been chosen, click "Solve…" to solve the system. Depending on how many wavefront sensors are used, the value of nshell and whether ray tracing is used, this may take awhile. After one iteration (by clicking solve), a new box will appear which will allow you to do multiple iterations at once. All the new mirror bending and rigid body motions are automatically entered into the LSST window at this point to be ready for iterations. If you do not wish to do iterations, you can click "reset perturbations to defaults."

Tip to make the computer run through the iterations faster: Right-click on "My Computer" and choose "Properties." Click on the "Advanced" tab and select "Settings" under "Performance." Then choose "Adjust for best performance" and apply.

5.3.2.19 Iterations

Only one iteration is required in the ideal world where the sensitivity matrix is known precisely, where the control system is completely linear, and where there is no noise. The ability to do multiple iterations was added to determine if there is walk-off. We look both at the rms bendings of the three mirrors versus iteration and at the rms changes in bendings of the three mirrors versus iteration. We have defined a metric for the rigid body misalignment. Using that metric, we look at the rigid body misalignment metric versus iteration and the rigid body misalignment metric for the changes in the rigid body motions versus iteration. This shows that the alignment strategy essentially converges in one iteration and that there is only a slight improvement in the second iteration. The alignment does not walk off.

A strong independent corroboration of the alignment strategy was sought. For this reason, after each iteration, the mirror deformations and rigid body motions are applied and ray traces are done for the parallel ray bundles for the wavefront sensors. This has shown that starting with a 1 mm rms spot radius, we can achieve a 10 micron spot radius. The ideal system has an average spot radius of about 3 microns over the field.

5.3.2.20 Results

There are a number of diagnostic windows that open up after running the program, depending on the conditions chosen. (Some windows won't open unless you are doing an iteration, mirror bending or rigid body motions or select "SVD diagnostics," "list U and V matrices," "list spot radii," etc.) I find some of them (in bold) are especially useful to examine.

- ABCD matrices
- a_rigid_body_reference_arrays
- Rigid_body_a_x_arrays…
- Rigid_body_a_x_change_arrays…
- a_mirror_motions_arrays
- N_matrix array
- Zernike transformation matrices
- **M_Matrix_Array**
  > For each WS (both fitted and nonfitted), there is a sensitivity matrix which describes the response of the wavefront sensor for various Zernikes that are observed. The sensitivity matrix has one part due

to the mirror deformations and another part due to the rigid body motions. The part due to the mirror deformations can either be calculated using the analytic Zernike transformations or by ray tracing. The rigid body motions part of the sensitivity matrix is always calculated by ray tracing. If some degrees of freedom are not allowed (either by choosing piston, tilt or focus not DOF in the DM DOF box or by entering "unselected Zernikes"), those respective columns will be zeroed for each mirror.

# of columns in each matrix: 3 (for the three mirrors)*$(nshell+1)^2$ + 3 (for the three CCD degrees of freedom of 2 tilts and a z motion) + NDIM_ZERO_EXTEND columns (+sometimes 3 extra columns of zeros->mistake)
# of rows in each matrix: $(nshell+1)^2$

Figure 1:Sample M matrix window with 6 WS, nshell=1 (so 4 Zernikes and 4 rows in each matrix) Piston is not allowed as DM DOF (As a result, the first column for each mirror is comprised of zeroes.)

- Wavefront sensor position arrays
- a arrays
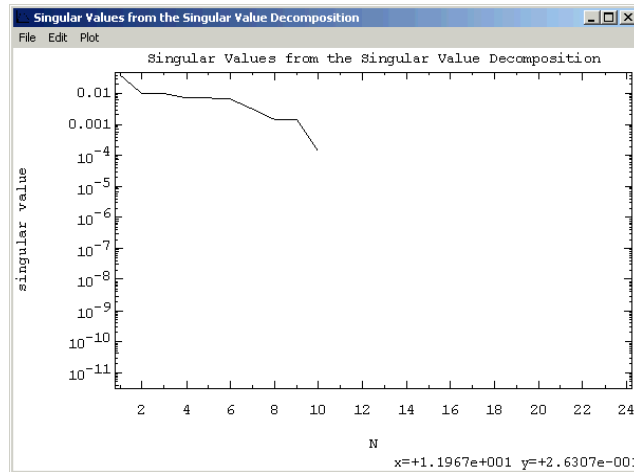- **Singular values from the singular value decomposition**

Figure 2: Plot of the singular values

- **Singular values**
  (List of the singular values. Make sure that the SVD max condition is set so as to include all the non-zero singular values.)
- SVD U and V matrices
- A_matrix, Ainv_matrix pseudo-inverse, Cgoal vector and Cachieved_vector arrays, C_vector and B vectors
- B Vector table in Excel format
- **Cgoal vector table in Excel format**
  The Cgoal vectors (one for each wavefront sensor) are the Zernike coefficients which describe the wavefront at each wavefront sensor location in the image. (Table includes list of the "Goal C vector array without errors," "Goal C vector array with errors," "Goal C error vector array," "Achieved C vector array," "Achieved C vector array - CGoal without errors vector array," "Achieved C vector array – Cgoal with errors vector array," "RMS error values before correction," "RMS error values after correction" and "RMS residual fraction arrays"
- **Original vs solved for mirror deformations**
  Comes from the B vectors
  Comparison of applied vs Solved for Zernike mirror coefficients – need not be exactly the same for a good solution
- **Original vs solved-for rigid body motion**
  Comparison of applied vs solved for rigid body motions – need not be exactly the same for a good solution
- Wavefront sensor circles on the LSST secondary mirror
- Wavefront sensor circles on the LSST tertiary mirror
- **Wavefront sensor RMS spot radii**
  Spot radii at each wavefront sensor before and after the last iteration completed are listed if "list WS spot radii" is checked. There are two columns for the number of rays attempted to be traced for each wavefront sensor and the number of unvignetted rays. Be sure that most (ideally all) of the rays are traced the whole

way. Otherwise, there will be incorrect (too small) values for the spot radii. The average radius calculation does not have any checks to exclude these incorrectly calculated small spot radii.

- **LSST setup summary**

    Lists setup conditions such as nshell, SVD max, bending or rigid body motions include, raytracing or analytic Zernike transformation formulas

    It'd be nice to have everything of interest recorded here… WS configuration name, type and amount of noise…

- **Misalignment measures and average WS rms wavefront**

    Includes mirror deformation RMS values and wavefront sensor average RMS after each iteration. One can observe the RMS bending at each mirror surface at each iteration and see that the solution may not require the mirror to bend less, but just in a different way to achieve good wavefronts across the field.   The solution may be evaluated by looking at the "fit ws avg" and "nonfat ws avg" to see the average departure from the wavefront that the ideal telescope would give. If wavefront sensors are chosen to be randomly omitted, the omitted wavefront sensors during each iteration are given in the final column of the table. Also, in this window, one can observe that even in the presence of large dynamic noise, the SVD finds nearly the same solution after each iteration, indicated by the relatively small changes listed for each of the three mirror bending deformations and rigid body motion.

- **Average spot radii at each iteration**

    (This only opens after iterating if list WS spot radii is checked.) Includes columns for "avg fitted cluster spot radius," "avg nonfitted cluster spot radius," "avg fitted image plane spot radius" and "avg nonfitted image plane spot radius." The cluster spot radii are calculated at the location where all the rays from one wavefront sensor come together the closest, which is at a different plane for each sensor. This is a useful diagnostic to make sure the software is working correctly, but not so useful for evaluating the telescope performance. It is better to evaluate system performance by looking at the image plane spot radii. The average spot radius is calculated separately for the fitted and nonfitted wavefront sensors. Also important is the shape of the spot in the image plane and diagnostics coming soon for this.

5.3.2.21 Number of wavefront sensors required

We have discovered that only five wavefront sensors are required for the case with piston unobservable. If good wavefronts are obtained for five wavefront sensors spread over the field, then it is guaranteed that the wavefronts are good across the entire field.

We have discovered that only three wavefront sensors are required for the case with piston and tilts unobservable. Less wavefront sensors are needed even though there is less information available because there are fewer modes on the mirrors that need to be corrected.

- Absolute minimum required to get good performance (but not necessarily the as-designed solution):
    – When piston and tilts are not observable:
        - For nshell = 2, you need 3 WFS
        - For nshell = 3, you need 4 WFS
        - For nshell = 4, you need 4 WFS
    – When piston only is not observable:
        - For nshell = 2, you need 4 WFS
        - For nshell = 3, you need 5 WFS
- More wavefront sensors may be used to improve performance with noise

This is true even if all the possible degrees of freedom are included as actual degrees of freedom. The possible degrees of freedom include the mirror deformations, the mirror rigid body motions, and the ccd motions for z and tip/tilt.

5.3.2.22 Getting back the input Zernike coefficients

The Zernike coefficients calculated might be different than the ones actually originally put on the mirrors, but you can take the difference of the two and propagate (raytrace) that to show that those null modes do not "mess up" the wavefront.

5.3.2.23 Spinoffs

The tomographic reconstruction work done for LSST led to the development of a diagnostic for reconstructing three-dimensional electron density profiles in plasmas. This work is chronicled in Appendix J.

Appendix J: K.L. Baker, "Tomographic reconstruction of high energy density plasmas with picosecond temporal resolution," accepted Opt Lett. (2005). UCRL number: UCRL-JRNL-215649

6) Exit Plan

The work on algorithms of interest to LSST has led to direct funding from that project and additional funding is expected for work on wave-front sensors applicable to this project